



## Full Text View

[Volume 28, Issue 6 \(June 1998\)](#)

### Journal of Physical Oceanography

Article: pp. 1252–1270 | [Abstract](#) | [PDF \(302K\)](#)

# Interdecadal Variability in a Zonally Averaged Ocean Model: An Adjustment Oscillator

**Jeff Drbohlav and Fei-Fei Jin**

*Department of Meteorology, School of Ocean and Earth Science and Technology, University of Hawaii at Manoa, Honolulu, Hawaii*

(Manuscript received October 23, 1996, in final form September 30, 1997)

DOI: 10.1175/1520-0485(1998)028<1252:IVIAZA>2.0.CO;2

## ABSTRACT

A meridional-plane, hemispherical ocean model is developed to study interdecadal variability of the thermohaline circulation (THC). The model differs from previous formulations of zonally averaged ocean models by using a prognostic equation to calculate the meridional velocity. This allows the incorporation of an adjustment timescale comparable to the advective timescale of the meridional overturning. An interdecadal oscillation is documented for an idealized ocean of homogeneous salinity forced by a time-independent surface heat flux.

The governing equations are linearized about a basic state in order to isolate the effect of parameter changes on the oscillation. An eigenvalue analysis reveals that the frequency of the oscillation is independent of the advective timescale. Instead, the interdecadal timescale of the oscillation is set by the slow adjustment of the overturning intensity to a meridional pressure gradient anomaly. The oscillatory instability, on the other hand, is dependent on both advective and adjustment processes. Advection by the basic state acts locally to reinforce the meridional pressure gradient anomaly, whereas the delayed adjustment of the overturning intensity to this pressure gradient anomaly modifies the poleward transport of heat, thereby initiating the phase reversal of the pressure gradient anomaly. Thus, the advection of temperature anomalies by the basic state provides a positive feedback while the adjustment of the overturning intensity serves as the phase-switching mechanism.

The relevance of this “adjustment oscillator” to the interdecadal variability simulated in idealized ocean general circulation models is discussed. The results strongly suggest that internal, interdecadal variability of the THC is not an inherently three-dimensional or nonlinear phenomenon and that this type of variability cannot be conceptualized as a loop oscillator.

### Table of Contents:

- [Introduction](#)
- [Model development and Interdecadal oscillation](#)
- [Eigenvalue analysis](#)
- [Physical mechanism](#)
- [Discussion](#)
- [REFERENCES](#)
- [FIGURES](#)

### Options:

- [Create Reference](#)
- [Email this Article](#)
- [Add to MyArchive](#)
- [Search AMS Glossary](#)

### Search CrossRef for:

- [Articles Citing This Article](#)

### Search Google Scholar for:

- [Jeff Drbohlav](#)
- [Fei-Fei Jin](#)

## 1. Introduction

Fluctuations in the intensity of the large-scale meridional overturning of the Atlantic Ocean, commonly referred to as the thermohaline circulation (THC), are believed to play a crucial role in climate dynamics. [Rooth \(1982\)](#) suggests that catastrophic transitions in the structure of the THC are capable of producing dramatic changes in the global climate system. [Stocker and Mysak \(1992\)](#) contend that natural climate variability within the coupled atmosphere–ocean–ice system, rather than external solar forcing, may be responsible for the interdecadal to centennial variability observed in proxy data records covering the past 10 000 years. The THC plays a fundamental role in climate variability because the intensity of the THC regulates the poleward transport of heat, thereby impacting the rate of sea ice formation and the atmosphere–ocean heat flux in the North Atlantic region (e.g., [Manabe and Stouffer 1988](#)).

While interdecadal to centennial scale climate variations involve numerous feedbacks within the land–atmosphere–ocean–ice system, both numerical modeling and observational studies have identified internal variability of the THC as a possible source of interdecadal variability. [Delworth et al. \(1993\)](#) found the mechanisms of interdecadal variability in a coupled ocean–atmosphere general circulation model (CGCM) to rely principally on oceanic processes. Using 100 years of marine observations in the North Atlantic region, [Kushnir \(1994\)](#) documented interdecadal, basin-scale sea surface temperature (SST) variations that did not appear to be maintained by coupled ocean–atmosphere interactions. Since the SST anomaly patterns identified by the two studies are somewhat similar, the combined results suggest that internal ocean dynamics play an important role in climate variability on interdecadal timescales.

Because internal ocean dynamics are believed to strongly influence the characteristics of interdecadal climate variability, several studies have attempted to isolate the basic mechanisms of THC variability in ocean models that are decoupled from the climate system. For instance, both [Chen and Ghil \(1995\)](#) and [Greatbatch and Zhang \(1995\)](#) assert that ocean general circulation models (OGCMs) forced by time-independent surface buoyancy fluxes are capable of producing interdecadal oscillations that have many similarities to the interdecadal variability simulated in a CGCM. Furthermore, [Greatbatch and Zhang \(1995\)](#) suggest that the oscillations are entirely thermally driven and can be explained in terms of a simple relationship between the strength of the meridional overturning and anomalous heat transport. In particular, they proposed that when the meridional overturning is strong, more heat is transported poleward. This decreases the meridional pressure gradient, thereby reducing the strength of the THC. The anomalously low poleward heat transport associated with a weak THC leads to high-latitude cooling that increases the meridional pressure gradient. This accelerates the meridional overturning and the process repeats itself. Similar mechanisms were proposed by [Huang and Chou \(1994\)](#) and [Chen and Ghil \(1995\)](#) for generating internal variability in OGCMs.

While this simple description of the oscillatory mechanism produces a clear picture of THC variability, it also neglects many fundamental issues. For instance, the adjustment of the THC is strongly constrained by geostrophy and, therefore, the intensity of anomalous overturning is determined by differences in zonal rather than meridional pressure anomalies. Thus, additional physics beyond geostrophy are required to explain the causal relationship between the meridional pressure gradient and overturning intensity. An elementary constraint of ocean circulation that may be responsible for this relationship is the blocking of normal flow by the boundaries of the ocean basin. For example, [Greatbatch and Peterson \(1996\)](#) suggest that the propagation of viscous, baroclinic Kelvin waves along the northern boundary of the OGCM is responsible for the phase lag between meridional pressure gradient anomalies and anomalous overturning. [Winton \(1996\)](#) discusses the impact of lateral boundaries on both stationary and oscillatory solutions of a coarse-resolution OGCM. Thus, the fundamental component of the oscillation is not a simple relationship, but rather a complicated function of boundary layer dynamics.

Another shortcoming of the oscillatory mechanism is that it describes the oscillation in terms of only a negative feedback. Thus, the physical mechanism is incomplete because some type of positive feedback is required to maintain the oscillation against the dissipation of density and momentum anomalies caused by mixing processes in the ocean. [Huang and Chou \(1994\)](#) suggest that the alternating positive and negative surface density anomalies associated with this type of variability might be consistent with those generated by a loop oscillator. The distinguishing feature of a loop oscillator is that a density anomaly circulates around a hypothetical loop repeatedly (e.g., [Dewar and Huang 1995](#)). As a result, the frequency of the oscillation is proportional to the time-mean overturning intensity. Huang and Chou, though, did not find this relationship to hold in a OGCM parameter sensitivity study. Thus, it is unclear whether the instability sustaining the interdecadal oscillations in the OGCM is related to that of a loop oscillator.

The purpose of this paper is to examine the essential components of this type of internal, interdecadal ocean variability. Instead of using an OGCM, the present study isolates the physical mechanism in a zonally averaged ocean model. A zonally averaged ocean model offers a unique opportunity to explore the mechanism of this oscillation because the inherently complex adjustment processes of the THC can be represented in a highly simplified manner. This facilitates the identification of the instability sustaining the oscillation. [Section 2](#) discusses the model development and parameters, while [section 3](#) examines one particular oscillation. [Section 4](#) presents an eigenvalue analysis of the sensitivity of the leading mode to variations in the adjustment parameters and specified basic state. [Section 5](#) describes the instability sustaining the oscillation,

and [section 6](#) concludes with a discussion on the relevance of this oscillatory mechanism to internal variability simulated in loop oscillator models and OGCMs.

## 2. Model development and parameters

To explore the dependence of THC internal variability on the adjustment timescale of the meridional velocity, a simple zonally averaged, hemispherical ocean model is developed. The model is highly idealized in that it assumes an ocean of constant and homogeneous salinity and no wind stress at the ocean surface. In addition, a time-independent surface heat flux is used to force the ocean circulation. Previous studies using similar surface boundary conditions have found interdecadal variability over a broad region of parameter space, but only in OGCMs ([Huang and Chou 1994](#); [Greatbatch and Zhang 1995](#); [Cai et al. 1995](#)). The lack of internal, decadal to interdecadal oscillations in zonally averaged ocean models has supported the notion that this type of variability is inherently three-dimensional.

However, the adjustment timescale of the THC has been distorted in the previous formulations of zonally averaged ocean models. First, even though several authors (e.g., [Rooth 1982](#); [Hasselmann 1991](#); [Marotzke 1994](#)) have suggested that the fluctuations in the THC strongly control the internal timescales of the climate system on decades to centuries, many zonally averaged ocean models (e.g., [Marotzke et al. 1988](#); [Yang and Neelin 1993](#); [Winton and Sarachik 1993](#)) use artificially large momentum damping rates that limit the adjustment timescale of the meridional velocity ( $\bar{\mathbf{U}}$  where overbars denote a zonal average) to a few months rather than decades. As a result, any variability that is dependent on an interaction between adjustment and advective processes is severely damped because adjustment processes dominate the evolution of the THC. Second, zonally averaged ocean models (e.g., [Wright and Stocker 1991](#)) that use physically reasonable momentum damping rates but still assume a diagnostic balance between  $\bar{\mathbf{U}}$  and the zonally averaged meridional pressure gradient ( $\bar{p}_y$ ) implicitly incorporate an adjustment timescale of  $\bar{\mathbf{U}}$  comparable to that of models that use artificially large momentum damping rates.

### *a. Previous studies using zonally averaged ocean models*

The main obstacle in developing a zonally averaged ocean model to simulate the THC is determining the east–west pressure difference. Since the adjustment timescale of the THC is much greater than the rotation rate of the earth, the meridional velocity will be nearly geostrophic and, thus, proportional to the east–west pressure difference. However, the east–west pressure gradient cannot be determined from the set of zonally averaged primitive equations, so this value must be parameterized in order to close the system of equations ([Marotzke et al. 1988](#)).

One approach to circumvent this obstacle is to consider a nonrotating fluid system and assume that the local time derivatives and inertial terms in the momentum equations are negligible. This results in an expression relating  $\bar{\mathbf{U}}$  to  $\bar{p}_y$ . The exact nature of the relationship depends on the closure approximation for momentum damping. [Marotzke et al. \(1988\)](#) used vertical Laplacian friction, whereas [Winton and Sarachik \(1993\)](#) chose Rayleigh friction. Both studies parameterized the resistance to meridional flow due to rotation on a sphere by using artificially large momentum damping coefficients. In order to constrain the rate of meridional overturning to that of estimates obtained from ocean measurements, Marotzke et al. set the vertical viscosity coefficient to  $600 \text{ m}^2 \text{ s}^{-1}$ , while Winton and Sarachik used  $(1.6 \text{ h})^{-1}$  as a linear damping rate. Such extreme values of momentum damping will lead to an adjustment of  $\bar{\mathbf{U}}$  on the order of months, rather than the more realistic adjustment timescale of decades.

Instead of considering a nonrotating fluid system, [Wright and Stocker \(1991](#), henceforth WS) parameterized the east–west pressure gradient ( $p_e - p_w$ ) in terms of  $\bar{p}_y$ , thereby eliminating the need to use artificially large momentum damping rates in their formulation. In a later paper, [Wright et al. \(1995\)](#) reviewed the dynamical basis for the preceding parameterization and improved the closure scheme by considering vorticity dynamics. The major improvement in the new parameterization, besides having a stronger dynamical foundation, is that it incorporated the influence of the large-scale pressure variations in determining the overturning circulation.

However, the parameterizations of the zonally averaged momentum equations by WS and [Wright et al. \(1995\)](#) lack an adequate representation of adjustment processes and, therefore, are more suitable for examining stationary solutions of the THC. The main problem is that both formulations assume a diagnostic balance between  $\bar{\mathbf{U}}$  and the local or large-scale meridional pressure gradient. As a result,  $\bar{\mathbf{U}}$  will instantaneously adjust to zonally averaged density anomalies. For example, Wright et al. suggest that a physically appealing result of their formulation is that in high latitudes the overturning circulation is essentially determined by the pole to equator density difference. While this seems reasonable for a stationary circulation, the relationship becomes quite distorted if the adjustment of  $\bar{\mathbf{U}}$  is considered because it implies that a negative (positive) density anomaly near the equator will instantaneously increase (decrease) the overturning intensity in the northern latitudes. The THC, though, does not adjust in this manner because  $\bar{p}_y$  is largely balanced by the zonally averaged zonal velocity,  $\bar{u}$ , thereby delaying the adjustment of  $\bar{\mathbf{U}}$ .

Therefore, even though the parameterizations of WS and Wright et al. use physically reasonable momentum damping rates, the adjustment of  $\mathbf{v}$  to a meridional pressure gradient perturbation is still extremely fast because a diagnostic relationship between  $\mathbf{v}$  and  $\bar{p}_y$  eliminates the phase lag between these two variables. In OGCMs, though, maximum (minimum) meridional overturning tends to follow maximum (minimum) surface density anomalies in the sinking region. For example, Fig. 5 (not shown) of [Greatbatch and Zhang \(1995\)](#) clearly depicts this delay between overturning intensity and surface density anomalies. [Chen and Ghil \(1995\)](#) also note this delay in their schematic diagram (Fig. 20, not shown) of the oscillatory mechanism of an OGCM. Thus, the adjustment timescale of the THC under present formulations of zonally averaged ocean models is distorted compared to that of OGCMs.

### b. Model formulation

The previous formulations of zonally averaged ocean models can be extended to include a slower adjustment timescale for  $\mathbf{v}$  by simply using a prognostic equation to calculate  $\mathbf{v}$ . With the Boussinesq approximation, the  $\mathbf{v}$  momentum equation reduces to (in Cartesian coordinates)

$$\frac{\partial \bar{v}}{\partial t} + \bar{v} \frac{\partial \bar{v}}{\partial y} + \bar{w} \frac{\partial \bar{v}}{\partial z} + f \bar{u} = -\frac{1}{\rho_o} \frac{\partial \bar{p}}{\partial y} + A_h \frac{\partial^2 \bar{v}}{\partial y^2} + A_v \frac{\partial^2 \bar{v}}{\partial z^2}, \quad (1)$$

where  $y(z)$  represents the meridional (vertical) coordinate;  $t$  denotes time;  $f$  is the Coriolis parameter;  $\rho_o$  is the mean density of ocean water; and  $A_h$  ( $A_v$ ) is a constant horizontal (vertical) eddy viscosity. After substituting  $\bar{u} = \bar{u}_G + \bar{u}_A$  and rearranging, (1) can be expressed as

$$\frac{\partial \bar{v}}{\partial t} + \bar{v} \frac{\partial \bar{v}}{\partial y} + \bar{w} \frac{\partial \bar{v}}{\partial z} = -f \bar{u}_A + A_h \frac{\partial^2 \bar{v}}{\partial y^2} + A_v \frac{\partial^2 \bar{v}}{\partial z^2}, \quad (2)$$

where  $\bar{u}_G$  ( $\bar{u}_A$ ) represents the geostrophic (ageostrophic) component of  $\bar{u}$  and by definition  $\bar{u}_G = -\bar{p}_y / \rho_o f$ .

The semiempirical relationship linking  $\bar{u}_A$  to  $\bar{p}_y$  formulated by WS is used as a closure approximation for  $\bar{u}_A$ . Substituting

$$\bar{u}_A = \frac{\mu \mathcal{E}}{\Omega \rho_o f} \frac{\partial \bar{p}}{\partial y} \quad (3)$$

into (2) results in a prognostic equation for calculating  $\mathbf{v}$

$$\frac{\partial \bar{v}}{\partial t} + \bar{v} \frac{\partial \bar{v}}{\partial y} + \bar{w} \frac{\partial \bar{v}}{\partial z} = -\frac{\mu \mathcal{E}}{\Omega \rho_o} \frac{\partial \bar{p}}{\partial y} + A_h \frac{\partial^2 \bar{v}}{\partial y^2} + A_v \frac{\partial^2 \bar{v}}{\partial z^2}, \quad (4)$$

where  $\Omega$  is the angular velocity of the earth,  $\mu$  represents a linear damping rate for  $\mathbf{v}$ , and  $\mathcal{E}$  is a closure parameter defined by WS. Since  $\mathcal{E}$  is proportional to  $(1.0 - u / u_G)$ , WS speculated that  $\mathcal{E}$  should generally be positive and vary spatially.

However, this study follows WS and takes  $\mathcal{E}$  to be constant rather than attempting to account for its spatial variability. As a result, (4) does not resolve any physical phenomena associated with the variation of the Coriolis parameter with latitude ( $\beta$  effect).

It is of interest to consider a short example to help illustrate some of the physics incorporated in (4). By neglecting inertial terms and substituting Rayleigh friction ( $-\mu \mathbf{v}$ ) for Laplacian friction, (4) can be reduced to

$$\frac{\partial \bar{v}}{\partial t} = -\mu \left[ \frac{\mathcal{E}}{\rho_o \Omega} \frac{\partial \bar{p}}{\partial y} + \bar{v} \right]. \quad (5)$$

If  $\mathcal{E}$  is assumed to be independent of  $\mu$ , then the steady-state overturning intensity of (5) is independent of momentum damping. This implies that the acceleration of  $\mathbf{v}$  associated with the frictionally induced ageostrophic current  $\bar{u}_A$  is exactly balanced by the deceleration caused by friction itself. Thus, the amount of momentum damping only determines the adjustment timescale of  $\mathbf{v}$  and has little control over the circulation intensity. This is consistent with results from coarse-resolution OGCMs in which the meridional overturning intensity is insensitive to the amount of momentum dissipation. For



example, [Winton \(1996\)](#) increased the horizontal viscosity by more than an order of magnitude in a coarse-resolution OGCM and found the midbasin meridional overturning to vary by only 4%.

It is possible to reduce [\(5\)](#) to a balance between  $\mathbf{v}$  and  $\bar{p}_y$  by choosing  $\mu$  large enough so that  $d\mathbf{v}/dt$  is negligible:

$$\bar{v} = -\frac{\varepsilon}{\rho_o \Omega} \frac{\partial \bar{p}}{\partial y}. \quad (6)$$

This relationship [\(6\)](#) is equivalent to that used in the zonally averaged model of [Winton and Sarachik \(1993\)](#) and in box models of the THC, but the interpretation is different. Instead of considering  $\Omega/\varepsilon \approx (1 \text{ h})^{-1}$  as an artificially large Rayleigh friction coefficient, [\(6\)](#) implies that for a steady-state balance only a small fraction of the meridional pressure gradient is balanced by  $\mathbf{v}$ . The momentum damping coefficient, on the other hand, is implicitly determined by assuming that  $d\mathbf{v}/dt$  is negligible.

For example, taking  $Y = 3 \times 10^6 \text{ m}$ ,  $D = 10^3 \text{ m}$ , and  $V = 4 \times 10^{-3} \text{ m s}^{-1}$  as characteristic length, depth, and velocity scales restricts the magnitude of  $A_h$  or  $A_v$  to

$$A_h \gg VY \approx 10^4 \text{ m}^2 \text{ s}^{-1} \quad (7a)$$

$$A_v \gg \frac{VD^2}{Y} \approx 10^{-3} \text{ m}^2 \text{ s}^{-1} \quad (7b)$$

if  $d\mathbf{v}/dt$  is assumed to be negligible in [\(4\)](#). Thus, a diagnostic relationship between  $\mathbf{v}$  and  $\bar{p}_y$  requires artificially large eddy viscosities in order for the  $\mathbf{v}$  momentum equation to be dynamically consistent. For instance, typical values of  $A_v$  are on the order of  $10^{-4} \text{ m}^2 \text{ s}^{-1}$ , while values of  $A_h$  for models that do not resolve the western boundary current are usually on the order of  $10^3 \text{ m}^2 \text{ s}^{-1}$ . Since this study is concerned with the physics of a weakly frictional system,  $d\mathbf{v}/dt$  must be retained.

An advantage of this new formulation is that the model is quite similar to those used in previous studies. Therefore, any changes in model behavior can be directly linked to the slower adjustment timescale. A limitation of this formulation, though, is that the adjustment timescale is uniform throughout the model domain. This is undesirable because the adjustment of the THC is strongly modulated by Kelvin waves along the ocean boundaries and Rossby waves in the ocean interior (e.g., [Döscher et al. 1994](#)). As a result, the adjustment timescale should probably vary with latitude since the phase speed of these waves is a function of latitude.

However, [Winton \(1996\)](#) notes that simulations using  $\beta$ -plane and  $f$ -plane configurations of a coarse-resolution OGCM produce internal oscillations that have basically the same characteristics. This implies that a uniform adjustment timescale can be used to investigate the physical mechanism of these oscillations. Indeed, allowing the adjustment timescale to increase linearly from the southern to the northern boundary of this zonally averaged ocean model has little impact on the basic characteristics of the interdecadal variability, although both the intensity and frequency of the oscillation increase for the latitude-dependent adjustment timescale. Therefore, a uniform adjustment timescale is used in this study because it allows for a simple representation of adjustment processes without severely distorting the oscillatory mechanism.

### c. Adjustment parameters

The unique aspect of this model is that each term on the right-hand side (rhs) of [\(4\)](#) is multiplied by a momentum damping coefficient of  $\mathbf{v}$  ( $\mu$ ,  $A_h$ , and  $A_v$ ). As a result, the tuning of the model's steady-state volume transport to match that estimated from ocean observations does not restrict the adjustment timescale of  $\mathbf{v}$ . Rather, the adjustment timescale of  $\mathbf{v}$  can be freely varied by multiplying the entire rhs of [\(4\)](#) by a momentum damping parameter (henceforth  $\gamma$ ). This allows an examination of the sensitivity of internal ocean variability to variations in the adjustment timescale. Note, though, that the inertial terms,  $\mathbf{v}\mathbf{v}_y$  and  $w\mathbf{v}_z$ , also contribute to the steady-state balance. Thus,  $\gamma$  not only controls the adjustment timescale of  $\mathbf{v}$ , but also the relative importance of the inertial terms. As a result, the overturning intensity is dependent on  $\gamma$ . To permit control over the overturning intensity without affecting the momentum damping rate, an additional parameter  $c$ , where  $c = \varepsilon/\varepsilon_0$  with  $\varepsilon_0 = 1.5$ , is introduced. This model formulation requires a larger value of  $\varepsilon$  compared to that used by WS ( $\varepsilon_0 = 0.5$ ) because the inertial terms contribute to the stationary balance.

### d. Model equations, boundary conditions, and parameters

By also considering an ocean of uniform depth and width along with the hydrostatic approximation, the following set of zonally averaged equations is obtained:

$$\frac{\partial \bar{v}}{\partial t} + \bar{v} \frac{\partial \bar{v}}{\partial y} + \bar{w} \frac{\partial \bar{v}}{\partial z} = \gamma \left[ -\frac{c\mu\epsilon_0}{\Omega\rho_o} \frac{\partial \bar{p}}{\partial y} + A_h \frac{\partial^2 \bar{v}}{\partial y^2} + A_v \frac{\partial^2 \bar{v}}{\partial z^2} \right] \quad (8)$$

$$\frac{\partial \bar{p}}{\partial z} = -\bar{\rho} g \quad (9)$$

$$\frac{\partial \bar{v}}{\partial y} + \frac{\partial \bar{w}}{\partial z} = 0 \quad (10)$$

$$\frac{\partial \bar{T}}{\partial t} + \bar{v} \frac{\partial \bar{T}}{\partial y} + \bar{w} \frac{\partial \bar{T}}{\partial z} = K_h \frac{\partial^2 \bar{T}}{\partial y^2} + K_v \frac{\partial^2 \bar{T}}{\partial z^2} + CA \quad (11)$$

$$\bar{\rho} = \rho_o - \alpha \bar{T}, \quad (12)$$

where  $g$  is the acceleration due to gravity;  $w$  is the vertical velocity;  $T$  denotes temperature;  $K_h$  and  $K_v$  are constant horizontal and vertical diffusion coefficients; and  $CA$  represents a convective adjustment scheme that results in complete vertical mixing whenever the stratification is locally unstable. The linear equation of state (12) calculates  $\bar{\rho}$  in units of kilograms per cubic meter with  $\rho_o = 1027.79 \text{ kg m}^{-3}$  and  $\alpha = 0.223 \text{ kg m}^{-3} \text{ K}^{-1}$ .

This study considers a rectangular ocean basin with a meridional length ( $L$ ), zonal width ( $W$ ), and depth ( $H$ ) of 6000 km, 5000 km, and 4 km respectively. Grid resolution is 200 km in the horizontal with 26 vertical levels varying in resolution from 30 m at the surface to 250 m at the bottom. At the northern and southern boundaries a no-slip boundary condition is used along with the condition of no material or energy fluxes. In addition, the northern boundary layer (region of sinking) is not resolved due to low horizontal resolution. No-stress and no-flux boundary conditions are applied at the ocean bottom:

$$\bar{v} = \bar{w} = 0, \quad \frac{\partial \bar{T}}{\partial y} = 0 \quad (\text{no slip, no flux: } y = 0, L) \quad (13a)$$

$$\frac{\partial \bar{v}}{\partial y} = 0 \quad (\text{unresolved boundary layer: } y \approx L) \quad (13b)$$

$$\frac{\partial \bar{v}}{\partial z} = 0, \quad \bar{w} = \frac{\partial \bar{T}}{\partial z} = 0 \quad (\text{no stress, no flux: } z = -H). \quad (13c)$$

The rigid-lid approximation, no wind stress, and either a restoring or time-independent heat flux are used for surface boundary conditions:

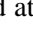
$$\bar{w} = 0, \quad \frac{\partial \bar{v}}{\partial z} = 0 \quad (\text{rigid lid, no wind stress}) \quad (14a)$$

$$K_v \frac{\partial \bar{T}}{\partial z} = \left\{ \frac{\eta(\bar{T}^* - \bar{T})}{Q_H} \right\}, \quad (\text{restoring condition}) \quad (14b)$$

where  $\eta$  is a relaxation timescale for heat,  $\bar{T}^*$  is the temperature to which SST is restored, and  $Q_H$  represents a time-independent heat flux.

Base values for model parameters are as follows:  $A_h = K_h = 3 \times 10^2 \text{ m}^2 \text{ s}^{-1}$ ,  $A_v = K_v = 10^{-4} \text{ m}^2 \text{ s}^{-1}$ ,  $\mu = 2 \times 10^{-10} \text{ s}^{-1}$ ,  $\epsilon_0 = 1.5$ ,  $\eta = (60 \text{ days})^{-1}$  for a 30-m surface layer, and time step dependent  $CA \approx 6 \text{ days}$ .


### 3. Interdecadal oscillation

The following section examines one particular oscillation to illustrate its characteristics. Model parameters are the same as the base values listed at the end of [section 2d](#) with  $Q_H$  ([Fig. 1](#) ) diagnosed from a steady-state circulation reached by restoring SST to


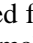

$$\bar{T}^* = 2 + 11.5 \times \left[ 1 + \cos\left(\frac{\pi y}{L}\right) \right], \quad (15)$$

where  $\bar{T}^*$  is in  $^{\circ}\text{C}$ . The parameters  $\gamma$  and  $c$  are set to 3.0 and 1.0 respectively. Thus, the adjustment timescale is roughly approximated by  $(\gamma\mu)^{-1} \approx 50 \text{ yr}$ . Since the model is only forced by a surface heat flux, the circulation will be hereafter referred to as the thermal circulation (TC).

#### a. Restoring boundary condition






[Figures 2a,b](#)  show the streamfunction,  $\Psi$  ( $\mathbf{u} = -\Psi_z$ ,  $w = \Psi_y$ ), and  $T$  (where overbars are here and hereafter dropped) of the stationary TC reached after 4000 years of integration by restoring SST to  $T^*$ . The salient feature of  $\Psi$  is the intense sinking at the northern boundary and upwelling throughout the rest of the ocean basin, while  $T$  is characterized by a pool of warm water overlying a relatively homogeneous, cool water mass. In addition, the parameters as chosen produce  $\Psi$  and  $T$  fields that are in reasonable agreement with observations of the North Atlantic Ocean.

#### b. Time-independent heat flux

At year 4000 an instantaneous heat flux was diagnosed from the stationary state of [Figs. 2a,b](#) . The model was subsequently restarted from the equilibrium state, but with the diagnosed heat flux ([Fig. 1](#) ) rather than the restoring condition as the thermal boundary condition. [Figures 3a,b](#)  show the time evolution of the strength of the meridional overturning and basin-average SST after the restart. The steady-state TC becomes unstable upon the switch from a restoring to flux boundary condition, but the oscillation amplitude is not resolved by the scale of the  $y$  axes.

To nudge the system away from the unstable stationary state, a  $+0.2^{\circ}\text{C}$  temperature anomaly is added to the upper 500 m poleward of  $40^{\circ}$  at year 4100. After the addition of the temperature perturbation, the system continues to evolve in an oscillatory manner with an increasing trend in frequency from roughly  $0.012$  to  $0.015 \text{ yr}^{-1}$  over the 2900-yr period shown. In addition, the TC drifts away from its original equilibrium state with the time-mean meridional overturning decreasing from 20.8 to 18.2 Sv ( $\text{Sv} \equiv 10^6 \text{ m}^3 \text{ s}^{-1}$ ) and basin-average SST increasing from  $13.5^{\circ}$  to  $14.0^{\circ}\text{C}$ . Approximately 4000 years after the addition of the temperature perturbation, the TC reaches a regular oscillation characterized by a period of 65.8 yr, basin-average SST extremes of  $14.39^{\circ}$  and  $13.56^{\circ}\text{C}$ , and overturning extremes of 22.9 and 14.3 Sv. The relatively long period of time required for the system to reach a regular oscillation implies that this oscillation is rather feeble. Therefore, the characteristics of this internal ocean variability are probably very sensitive to the numerous feedbacks within the coupled ocean–atmosphere–ice system.

#### c. Oscillation

The time-mean streamfunction  $\hat{\Psi}$  and temperature  $\hat{T}$ , where carets denote the time-mean of the zonal average, are displayed in [Figs. 4a,b](#)  for one complete oscillation beginning at year 8643.9 and ending at year 8709.7. The major features of  $\hat{\Psi}$  and  $\hat{T}$ , the intense sinking at the northern boundary and upwelling elsewhere and the pool of light water overlying a relatively homogeneous, dense water mass, are qualitatively similar to the equilibrium state described in [section 3a](#). However,  $\hat{\Psi}$  ([Fig. 4a](#) ) is weaker and shallower compared to the steady-state  $\Psi$  ([Fig. 2a](#) ). The shoaling of the TC confines the flow feeding the region of sinking to a shallower surface layer and reduces considerably the time-mean transport below the depth of 3000 m. The only notable difference between  $\hat{T}$  ([Fig. 4b](#) ) and the steady-state  $T$  ([Fig. 2b](#) ) is that the water above 1000 m is warmer and the deep ocean is slightly cooler.

To illustrate the extreme states of the oscillation the instantaneous  $\Psi$  and  $T$  are shown in [Figs. 5a–d](#)  for the maximum

(year 8663.2) and minimum (year 8688.9) overturning intensity. A reverse cell in both extreme states is present in the lower half of the basin but at different meridional locations. It will be shown later that the reverse cell originates at the northern boundary and propagates southward. The other notable feature is the large displacement between 40° and 55° of the  $T = 3^\circ\text{C}$  isothermal surface. It has a positive slope when overturning at the northern boundary is at a maximum, whereas it has a negative slope when overturning is at a minimum. Thus, the displacement of the  $T = 3^\circ\text{C}$  isothermal surface is strongly correlated with the strength of upwelling.

The characteristics of the oscillation are best illustrated by examining the anomalous (departure from time mean) streamfunction  $\Psi'$  and temperature  $T'$  fields. [Figures. 6a-l](#) display  $\Psi'$  and  $T'$  in 10.9-yr intervals spanning one complete oscillation. Clearly  $\Psi'$  depicts a southward propagating perturbation with the largest overturning anomalies at the northern boundary;  $T'$  also shows a southward propagating perturbation throughout the layer between roughly 300 m and 1000 m. In this layer  $T'$  appears to be largely dependent on the southward propagating vertical velocity at the base of the thermocline ( $\sim 1000$  m) with anomalous sinking (upwelling) producing a positive (negative) temperature anomaly. Note that this coupling cannot occur in models that require  $\mathbf{v}$  to balance  $p_y$ , since a positive (negative)  $T'$  would lead to a rapid adjustment to anomalous upwelling (sinking).

In addition to the southward propagating anomalies, several other features in the  $\Psi'$  and  $T'$  fields are noteworthy. In the upper 300 m  $T'$  propagates northward, thereby producing a “wrapping” of temperature anomalies in the upper 1000 m. The mechanism largely responsible for this process is the formation of “new” anomalies by the anomalous heat transport associated with the adjustment of the TC overturning intensity rather than the advection of “old” temperature anomalies by the basic-state flow. This is clearly shown by following the negative  $T'$  in the lower 3000 m of the model ocean beginning at year 8643.9 ([Fig. 6b](#)). After the surface water characterized by  $-T'$  sinks at the northern boundary, it is slowly advected southward in the lower 3000 m ([Figs. 6d.f.h.j.l](#)). Note, though, that after one complete oscillation (returning to [Fig. 6b](#)), the main portion of the temperature anomaly is located in the deep ocean between 5° and 25° latitude. Thus, the temperature anomaly is not advected completely around the domain in one period. Therefore, the physical mechanism producing the oscillation is quite different than that of the classic loop oscillator in which a density anomaly can be traced as it passes through a loop (e.g., [Dewar and Huang 1995](#)).

It is interesting that while  $\Psi'$  decays as it propagates southward,  $T'$  in the upper 1000 m amplifies upon reaching the southern boundary. Near the southern boundary above the base of the thermocline  $T'$  increases because the vertical temperature gradient in this region is so large that even a small  $\Psi'$  can produce a substantial  $T'$ . Below 1000 m, though, the  $T'$  becomes rather diffuse as it is advected southward from the sinking region. Even though the magnitude of  $T'$  below the thermocline is relatively small, the vertical extent of the deep-ocean  $T'$  is roughly three times larger than that of the upper-ocean  $T'$ . Therefore, the temperature anomalies in the northern part of the deep ocean are still an important component of the meridional pressure gradient force and, as a consequence, are an integral part of the adjustment process.

#### 4. Eigenvalue analysis

The main goal of this section is to examine the role of the TC adjustment in producing internal, interdecadal variability by determining the sensitivity of the oscillation to variations in model parameters. To isolate the effect of parameter changes on the oscillation characteristics, [\(8\) through \(12\)](#) are linearized about a basic state:

$$\begin{aligned} \frac{\partial \mathbf{v}'}{\partial t} + \hat{\mathbf{u}} \cdot \nabla \mathbf{v}' + \mathbf{u}' \cdot \nabla \hat{\mathbf{v}} \\ = \gamma \left[ -\frac{c\mu\epsilon_0}{\Omega\rho_o} \frac{\partial p'}{\partial y} + A_h \frac{\partial^2 \mathbf{v}'}{\partial y^2} + A_v \frac{\partial^2 \mathbf{v}'}{\partial z^2} \right] \end{aligned} \quad (16)$$

$$\frac{\partial p'}{\partial z} = -\rho' g \quad (17)$$

$$\frac{\partial \mathbf{v}'}{\partial y} + \frac{\partial \mathbf{w}'}{\partial z} = 0 \quad (18)$$

$$\frac{\partial T'}{\partial t} + \hat{\mathbf{u}} \cdot \nabla T' + \mathbf{u}' \cdot \nabla \hat{T} = K_h \frac{\partial^2 T'}{\partial y^2} + K_v \frac{\partial^2 T'}{\partial z^2} \quad (19)$$

$$\rho' = -\alpha T', \quad (20)$$



where primes (carets) denote time-dependent (time independent) quantities,  $\mathbf{u} = v\mathbf{j} + w\mathbf{k}$ , and

$$\nabla = \mathbf{j}\frac{\partial}{\partial y} + \mathbf{k}\frac{\partial}{\partial z}.$$

The growth rate and frequency of the leading mode are determined by solving for the eigenvalues of the discretized linear system using 13 vertical levels instead of the original 26. The reduction of vertical levels decreases computational requirements without significantly affecting the results.

A potential shortcoming of this method is that convective adjustment (CA) was neglected in the transformation of (11) into its linear equivalent (19). However, CA is relatively weak during the oscillation with the deepest convective overturning at the northern boundary reaching a depth of only 1600 m. As a result, CA has only a minor impact on the oscillation characteristics and, therefore, neglecting it does not distort the oscillatory mechanism. For instance, the time evolution of  $\Psi'$  and  $T'$  depicted in Figs. 6a–l is quite similar to the oscillation described by the dominant eigenvalue (growth rate =  $7.1 \times 10^{-4} \text{ yr}^{-1}$ , frequency =  $1.5 \times 10^{-2} \text{ yr}^{-1}$ ) and corresponding eigenvector of (16) through (20) when the basic state is set to the time-mean state of the oscillation in section 3.

The linearized inertial terms ( $\hat{\mathbf{u}} \cdot \nabla \mathbf{v}' + \mathbf{u}' \cdot \nabla \hat{\mathbf{v}}$ ) can also be neglected without distorting the oscillation characteristics. For example, Figs. 7a–f display the spatial pattern of  $\Psi'$  and  $T'$  at intervals of  $\pi/3$  (9 yr) for the leading mode with the inertial terms neglected. While both the growth rate ( $26.4 \times 10^{-4} \text{ yr}^{-1}$ ) and frequency ( $1.85 \times 10^{-2} \text{ yr}^{-1}$ ) increased, a comparison of Figs. 7a–f and 6a–f reveals that the spatial characteristics of  $\Psi'$  and  $T'$  remained essentially unchanged. The only notable contrast is in the upper-ocean  $T'$  near the sinking region where convection is important in determining the spatial structure of  $T'$ . As mentioned earlier, this difference has only a minor influence on the oscillatory mechanism. Therefore, both convective adjustment and the inertial terms play an insignificant role in the oscillatory mechanism.

An underlying assumption of the following eigenvalue analysis is that the specified basic state is a stationary state of (8) through (12). Note, though, that as long as the specified basic state does not violate the continuity equation and hydrostatic approximation, then it fulfills this requirement because a time-independent forcing that makes the basic state stationary can be diagnosed from (8) and (11). Although the ocean circulation is primarily driven by fluxes of momentum and heat through its surface, this procedure allows the forcing to be distributed throughout the entire model domain. The advantage in allowing the forcing to be distributed in this manner is that the sensitivity of the oscillation to variations in the basic state and model parameters can be separated. For example, as the parameter  $c$  is increased in the nonlinear model, both the time-mean overturning intensity and oscillation frequency increase. Thus, it is unclear whether the increase in frequency is caused by the change in overturning intensity and/or  $c$ . With a “distorted forcing” eigenvalue analysis, the basic state can be kept constant as  $c$  is varied and vice versa, thereby enabling the relative influence of the variations in  $c$  and the basic-state overturning intensity on the frequency to be determined.

### a. Adjustment parameter sensitivity

The sensitivity of the growth rate and frequency to variations in  $\gamma$  and  $c$  is determined by calculating the eigenvalues of the linear system (16) through (20) with the basic-state variables  $\hat{u}$  and  $\hat{T}$  set to the unstable stationary state (Figs. 2a,b) reached by restoring SST to  $T^*$ . Figures 8b and 9b clearly indicate that the frequency of the leading mode increases as the square root of both  $\gamma$  and  $c$ . This suggests that the magnitude of the first term on the rhs of (16) is largely responsible for setting the frequency of the oscillation. The growth rate, however, exhibits distinct sensitivities to the two adjustment parameters. With respect to  $\gamma$  (Fig. 8a), it is bounded by a maximum of  $1.5 \times 10^{-3} \text{ yr}^{-1}$  at  $\gamma \approx 2.0$  and positive only over the range of  $0.9 < \gamma < 4.0$ . On the other hand, the growth rate is an increasing function of  $c$  (Fig. 9a). Variations in  $\gamma$  and  $c$  affect the growth rate differently because  $c$  controls the local sensitivity of  $\mathbf{v}'$  to a given  $p'_y$ , whereas  $\gamma$  governs the nature of the large-scale adjustment of the TC.

### b. Basic-state sensitivity

The oscillation is also sensitive to changes in the basic state. For example, the oscillation period decreases from 80.5 to 65.8 yr when the basic state is switched from the unstable stationary state (Figs. 2a,b) to the time-mean state (Figs. 4a,b). Note that the period of the oscillation is longer for the stationary state even though its meridional overturning is stronger than the time-mean state. This suggests that the frequency is not strongly controlled by the intensity of the basic-state flow. To emphasize the independence of the frequency and advective timescale, the growth rate and frequency are computed with the basic-state variables set to the unstable stationary state (symbolically denoted as  $\hat{\mathbf{u}}_o$  and  $\hat{T}_o$ ), but with either  $\hat{\mathbf{u}}_o$  or  $\hat{T}_o$  multiplied by an arbitrary factor  $\delta$  over the entire model domain (Figs. 10a,b). Remarkably, for a fourfold increase in basic-state overturning intensity, the oscillation frequency remains relatively unchanged. In contrast, the frequency doubles

for a fourfold increase in the basic-state density stratification. The sensitivities of the growth rate with respect to  $\delta\hat{u}_o$  and  $\delta\hat{T}_o$  are also quite different. The growth rate is an increasing function of  $\delta\hat{T}_o$  whereas it is bounded with respect to  $\delta\hat{u}_o$ .

These results highlight two important components of the oscillation. First, the growth rate is sensitive to modifications of the basic-state overturning intensity. Therefore, both adjustment and advective processes are important in generating the instability. Second, the frequency of the oscillation is independent of the basic-state overturning intensity, but increases as the square root of the basic-state density stratification. This indicates that the frequency of the oscillation is strongly controlled by the rate at which the meridional velocity adjusts to pressure gradient anomalies.

## 5. Physical mechanism

[Figure 11](#) displays a schematic diagram of the oscillation for the northern part of the model domain. The dashed line separates the ocean into two distinct regions based on the temperature structure of the basic state. In the upper 1000 m,  $\hat{T}_y < 0$  and  $\hat{T}_z > 0$ , whereas  $\hat{T}_y \approx \hat{T}_z \approx 0$  in the lower 3000 m. Thus, anomalous overturning only affects the heat balance of the upper ocean. In addition, the heat transport by  $w'$  is assumed to be negligible compared to that by  $\mathbf{V}'$ . This assumption is only valid for  $y > 50^\circ$  since [Fig. 6](#) clearly shows that in the upper ocean, large negative (positive) temperature anomalies tend to be associated with anomalous upwelling (sinking).

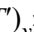


The oscillation is taken to start with a minimum  $T'$  in the upper ocean, a minimum  $T'$  in the deep ocean near the sinking region, and a maximum  $T'$  away from the sinking region ([Fig. 11a](#)). Note that the  $T'$  structure in the deep ocean produces a strong negative temperature gradient anomaly. This accelerates the meridional overturning that, consequently, increases the poleward transport of heat in the upper ocean. When the anomalous overturning reaches a maximum ([Fig. 11b](#)), the negative temperature anomaly in the upper ocean has been neutralized by the stronger than normal heat transport associated with the enhanced overturning. In addition, the minimum  $T'$  in the deep ocean has been advected southward by the basic-state flow. Because the system is weakly frictional, the anomalous overturning overshoots this potential equilibrium state, thereby resulting in a positive temperature anomaly in the upper ocean. Furthermore, a fraction of this upper-ocean  $T'$  sinks at the northern boundary and the negative  $T'$  in the deep ocean continues to be advected southward. As a result, the enhanced overturning is decelerated due to this developing positive temperature gradient anomaly. When the overturning anomaly is finally reduced to zero ([Fig. 11c](#)), both the temperature anomaly in the upper ocean and the temperature gradient anomaly in the deep ocean are at their maximum values of the oscillation. The strong positive temperature gradient anomaly continues to force the overturning perturbation to its negative phase and the oscillation proceeds as discussed above, but in the opposite sense.


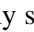
This description of the oscillatory mechanism is similar to that suggested by several authors (e.g., [Greatbatch and Zhang 1995](#); [Huang and Chou 1994](#); [Chen and Ghil 1995](#)) for producing internal variability in an OGCM in that it is based on a negative feedback between the strength of the overturning intensity and the meridional pressure gradient anomaly. Thus, the mechanism is incomplete because some type of positive feedback is required to sustain the oscillation against the damping of momentum and temperature anomalies by mixing processes in the ocean. However, the phase relationship between the temperature anomaly in the upper ocean and the temperature gradient anomaly in the deep ocean suggests that the advection of temperature anomalies by the basic state can trigger an instability.

For example, in [Fig. 11a](#) the  $T'$  in the upper ocean is a minimum and, therefore,  $\nabla^2 T'_{yy}$  is a maximum since the Laplacian of a function tends to be a maximum (minimum) where the function itself is a minimum (maximum). Thus, the advection of the upper-ocean  $T'$  by the basic state is acting to decrease (increase)  $T'_y$  in [Fig. 11a](#) ([Fig. 11c](#)). More importantly, the basic-state advection of  $T'$  is actually reinforcing the vertically integrated temperature gradient anomaly,  $\langle T'_y \rangle$  (where  $\langle [ ] \rangle$  represents  $\int_{-H}^0 [ ] dz$ ), because near the sinking region  $\langle T'_y \rangle$  is largely determined by the temperature gradient anomaly in the deep ocean. Since the intensity of the overturning perturbation is dependent on the magnitude of  $\langle T'_y \rangle$ , the forcing of  $\langle T'_y \rangle$  by the basic-state advection of  $T'$  (symbolically denoted by a bold arrow in [Fig. 11](#)) induces a stronger overturning anomaly compared to the previous adjustment phase. As a result, the anomalous heat transport associated with this overturning perturbation is greater than that of the previous phase, thereby causing the magnitude of the upper-ocean  $T'$  to increase a half cycle later. This, in turn, leads to a stronger temperature gradient anomaly in the deep ocean because the upper-ocean  $T'$  sink at the northern boundary. In addition, the strength of the forcing of  $\langle T'_y \rangle$  by the basic-state advection of  $T'$  is enhanced due to the increased magnitude of the upper-ocean  $T'$ . This induces yet another overturning anomaly that is stronger than the previous one and, therefore, the intensity of the oscillation continues to increase until nonlinear effects become important.


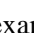


This conceptual view of the oscillatory mechanism highlights two important components of the oscillation. First, the internal variability originates due to an interaction between advective and adjustment processes. In particular, the advection of temperature anomalies by the basic state acts locally to enhance the meridional pressure gradient anomaly, whereas the delayed adjustment of the overturning intensity to this pressure gradient anomaly modifies the poleward transport of heat thereby initiating the phase reversal of the pressure gradient anomaly. Second, the evolution of the deep-ocean temperature anomalies near the sinking region is extremely important because the pressure gradient anomaly produced by the deep-ocean temperature anomalies is largely responsible for inducing the overturning perturbation. The remainder of this section examines these two aspects of the oscillation in greater detail by analyzing the eigenvectors of the eigenvalue analysis presented in [section 4](#).

### a. Instability mechanism

The advection of temperature anomalies by the basic state ( $\hat{\mathbf{u}} \cdot \nabla T'$ ) triggers an instability by instantaneously reinforcing the meridional pressure gradient anomaly. After applying boundary conditions, the feedback between  $p'_y$  and  $\hat{\mathbf{u}} \cdot \nabla T'$  can be represented by the phase relationship between the vertically integrated temperature gradient anomaly,  $\langle T'_y \rangle$ , and the forcing of  $\langle T'_y \rangle$  by the basic-state advection of  $T'$ ,  $\langle -(\hat{\mathbf{u}} \cdot \nabla T')_y \rangle$ . [Figure 12](#)  displays this phase relationship for the base ( $\gamma = 3$ ,  $c = 1$ ),  $c = 4$  ( $\gamma = 3$ ), and  $\gamma = 12$  ( $c = 1$ ) oscillations. A positive feedback occurs when  $\langle T'_y \rangle$  and  $\langle -(\hat{\mathbf{u}} \cdot \nabla T')_y \rangle$  vary in phase (i.e., between  $\pm 90^\circ$ ) and, therefore, the feedback is positive only in the northern part of the model domain. The location where  $\langle -(\hat{\mathbf{u}} \cdot \nabla T')_y \rangle$  starts to lag  $\langle T'_y \rangle$  by more than  $90^\circ$  (negative feedback) is associated with the damping of overturning anomalies. Consequently,  $\Psi'$  of the base oscillation propagates past  $y = 40^\circ$  without being damped considerably, whereas the  $\Psi'$  of both the  $c = 4$  and  $\gamma = 12$  oscillations decrease in this region. For example, a comparison of the  $\Psi'$  spatial pattern of the  $\gamma = 12$  oscillation ([Figs. 13a,b](#) ) with that of the base oscillation (e.g., [Figs. 7a,c](#) ) illustrates this difference in  $\Psi'$  propagation. Note that the  $\Psi'$  of the  $\gamma = 12$  oscillation is confined closer to the sinking region even though the eddy viscosities are four times greater for the  $\gamma = 12$  than the base oscillation.



Therefore, the characteristics of  $\Psi'$  propagation are strongly influenced by this advective feedback. Note, though, that the strength of feedback is not only dependent on the phase relationship between  $\langle T'_y \rangle$  and  $\langle -(\hat{\mathbf{u}} \cdot \nabla T')_y \rangle$ , but also the relative magnitude of these terms. To illustrate the spatial variability of the feedback strength, [Figs. 14a,b,c](#)  display a phase diagram of  $\langle T'_y \rangle$  and  $\langle -(\hat{\mathbf{u}} \cdot \nabla T')_y \rangle$  at  $y = 50^\circ$  and  $y = 40^\circ$  for the base,  $c = 4$ , and  $\gamma = 12$  oscillations respectively. It is interesting that even though the  $\gamma = 12$  oscillation has a relatively strong positive feedback at  $y = 50^\circ$  ([Fig. 14c](#) ) its growth rate is still negative ( $-1.6 \times 10^{-2} \text{ yr}^{-1}$ ). This indicates that the mechanism of the oscillation is not solely dependent on this advective feedback. Indeed, the sensitivity of the overturning intensity to a given pressure gradient anomaly is also very important in triggering the instability because it determines the degree of coupling between advective and adjustment processes.

For example, if  $\mathbf{v}'$  is sensitive to  $p'_y$ , then a positive feedback between  $\langle T'_y \rangle$  and  $\langle -(\hat{\mathbf{u}} \cdot \nabla T')_y \rangle$  will induce a stronger overturning anomaly compared to if the positive feedback was absent. This, in turn, increases the anomalous heat transport associated with the delayed adjustment of  $\mathbf{v}'$ , thereby resulting a half cycle later in temperature anomalies above the thermocline that are opposite in sign and greater in magnitude than the original  $T'$ . The increase in magnitude of the upper-ocean  $T'$  has two important effects. First, it supplies the sinking region at the northern boundary with larger temperature anomalies, thereby increasing the magnitude of the temperature gradient anomaly in the deep ocean. Second, it enhances the strength of the forcing of the pressure gradient anomaly by the basic-state advection of upper-ocean temperature anomalies. As a result, the system exhibits oscillatory behavior. On the other hand, if  $\mathbf{v}'$  is relatively insensitive to  $p'_y$  (no interaction between adjustment and advective processes), then a positive feedback between  $\langle T'_y \rangle$  and  $\langle -(\hat{\mathbf{u}} \cdot \nabla T')_y \rangle$  has only a marginal impact on the TC adjustment. Thus, the anomalous heat transport is independent of the positive feedback and, therefore, the adjustment process does not increase the magnitude of the upper-ocean  $T'$ . Indeed, the  $T'$  are continuously damped by diffusion, thereby causing the oscillation amplitude to decrease.

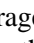
The significance of the interaction between adjustment and advective processes can be illustrated by comparing the sensitivity of the oscillation to different closure approximations for momentum damping. For instance, when horizontal viscosity is neglected ( $A_h = 0$ ), the range of positive growth rates expands sharply from  $0.9 < \gamma < 4.0$  ([Fig. 8a](#) ) to  $0.7 < \gamma < 24.0$  ([Fig. 15](#) ). In addition, the maximum growth rate increases by almost an order of magnitude. To examine why horizontal viscosity has a strong impact on the stability of the oscillation, the phase lag between  $\langle -T'_y \rangle$  and  $\langle \mathbf{v}' \rangle_u$  (where  $\langle \mathbf{v}' \rangle_u$  represents  $\int_{-1.2}^0 [ \ ] dz$ ) is displayed for variations in  $\gamma$  for both  $A_h = 0$  ([Fig. 16a](#) ) and standard ([Fig. 16b](#) )

conditions. The phase relationship is roughly constant for variations in vertical viscosity with  $\langle -T'_y \rangle$  leading  $\langle \mathbf{V}' \rangle_u$  by roughly  $90^\circ$  and, therefore,  $\mathbf{V}'$  is tightly coupled to  $p'_y$ . On the other hand, the phase relationship near the sinking region becomes distorted as  $A_h$  increases because the relatively strong response of  $\mathbf{V}'$  at the sinking region is spread rapidly southward by the horizontal viscosity. For example,  $\langle \mathbf{V}' \rangle_u$  reaches a maximum before  $\langle -T'_y \rangle$  around  $y = 50^\circ$  for the  $\gamma = 24$  oscillation and, therefore, the local forcing of  $\mathbf{V}'$  by  $p'_y$  is marginal compared to the remote forcing of  $\mathbf{V}'$  by  $\gamma A_h \mathbf{V}'_{yy}$ . Thus, the oscillation is severely damped for large values of horizontal viscosity because the local forcing of the temperature gradient anomaly by the basic-state advection of temperature anomalies has a negligible effect on the adjustment of the meridional overturning.

### b. The importance of deep-ocean $T'$

Even though the magnitude of the deep-ocean  $T'$  is smaller than that of the upper-ocean  $T'$  (e.g., [Fig. 6](#) ) , the deep-ocean  $T'$  still plays a fundamental role in the instability. For example, the relative contribution of the deep  $T'_y$  ( $\langle T'_y \rangle_d$  where  $\langle \cdot \rangle_d$  represents  $\int_{-H}^{-1.2} [\cdot] dz$ ) to  $\langle T'_y \rangle$  easily exceeds that from  $\langle T'_y \rangle_u$  at  $y = 50^\circ$  for the base oscillation ([Fig. 17](#) ) . The deep-ocean  $T'$  dominates  $p'_y$  near the sinking region because of its long vertical extent and strong gradient in the meridional direction. As a result, the deep-ocean  $T'$  induces an adjustment of the overturning intensity as it slowly moves southward from the sinking region. Thus, the temperature anomalies do not have to “circle around a loop” in order to produce internal variability because the deep-ocean  $T'$  indirectly affects the heat balance of the upper ocean by modifying the meridional overturning intensity. Therefore, the period of this oscillation is shorter than that of an oscillation produced by the loop oscillator mechanism. For instance, [Winton and Sarachik \(1993\)](#) identified an oscillation in a zonally averaged ocean model of the loop oscillator type that had a period of roughly 500 yr, about an order of magnitude greater than the characteristic period of this type of oscillator.

As a result of its strong influence on both  $\langle T'_y \rangle$  and the upper-ocean  $T'$ , the deep-ocean  $T'$  is a crucial component of this oscillation and, consequently, the feedback between  $\langle T'_y \rangle$  and  $\langle -(\hat{\mathbf{u}} \cdot \nabla T')_y \rangle$ . Indeed, this feedback turns negative where the deep-ocean  $T'$  becomes marginal in determining  $\langle T'_y \rangle$ . The main reason for this relationship is that the leading term of  $-(\hat{\mathbf{u}} \cdot \nabla T')_y$  is  $-\hat{\mathbf{u}} T'_{yy}$  and, therefore, a positive feedback is dependent on  $T'_y$  and  $-(\hat{\mathbf{u}} \cdot \nabla T')_y$  being in phase at different depths. Since  $\langle -\hat{\mathbf{u}} T'_{yy} \rangle$  is largely determined by the upper-ocean  $T'$  while  $\langle T'_y \rangle$  is strongly influenced by the deep-ocean  $T'$ , a positive feedback is characterized by maximum (minimum) upper-ocean temperature anomalies being located above maximum (minimum) deep-ocean temperature gradient anomalies. This vertical structure of  $T'$  is consistent with  $\langle \mathbf{V}' \rangle_u$  lagging  $\langle -T'_y \rangle$  by roughly  $90^\circ$  since the anomalous heat transport associated with the adjustment of the overturning intensity dictates the evolution of the upper-ocean  $T'$ . Thus, the delayed adjustment of  $\mathbf{V}'$  to  $p'_y$  is crucial for producing the instability. As a result, zonally averaged ocean models that are based on a diagnostic balance between  $\mathbf{V}$  and  $p_y$  will not simulate this type of internal, interdecadal variability.

It is important to note, though, that while adjustment processes determine the time evolution of the upper-ocean  $T'$ , advection strongly controls the evolution of the deep-ocean  $T'$ . Therefore, the adjustment timescale needs to be comparable to the advective timescale in order to produce a  $T'$  vertical structure favorable for a positive feedback. For example, the instability is favored at stronger rates of momentum damping (faster adjustment) as the overturning intensity increases ([Fig. 15](#) ) . Thus, the instability is not solely dependent on the slow dynamical adjustment of this zonally averaged ocean model. Rather, the oscillation is only unstable for slow adjustment timescales because of the limitation imposed by the advective timescale of the model TC.

## 6. Discussion

The physical mechanism responsible for producing internal, interdecadal variability in this zonally averaged ocean model can best be described as an adjustment oscillator. The adjustment oscillator relies on an interaction between advective and adjustment processes to trigger an instability. Near the sinking region the advection of upper-ocean temperature anomalies by the basic state acts locally to reinforce the meridional pressure gradient anomaly set by the temperature anomalies in the deep ocean. The delayed adjustment of the overturning intensity to this pressure gradient anomaly alters the poleward transport of heat, thereby reversing the phase of the temperature anomalies in the upper ocean. This, in turn, changes the phase of the pressure gradient anomaly in the deep ocean because the upper-ocean temperature anomalies sink at the northern boundary. Thus, advection by the basic state produces a positive feedback whereas the adjustment of the overturning intensity serves



as the phase-switching mechanism. The interdecadal timescale of the oscillation is set by the slow adjustment of the overturning intensity to a meridional pressure gradient anomaly.

The instability of an adjustment oscillator is quite different than that of a loop oscillator. A loop model does not exhibit this type of variability because it does not resolve the positive feedback involving the basic-state advection of temperature anomalies and, in addition, the fluid velocity must adjust simultaneously throughout the entire loop. An OGCM, on the other hand, should be able to resolve the basic components of the adjustment oscillator. However, it is difficult to predict the role that this oscillatory mechanism might play in the interdecadal variability simulated in OGCMs because of the assumptions involved in reducing the three-dimensional TC to a meridional plane. Most importantly, a zonally averaged ocean model assumes that it is possible to average two unlike quantities, the western boundary current and the ocean interior, and still obtain a meaningful average. As a result, the details of this instability may be slightly distorted for a three-dimensional TC. However, several components of this adjustment oscillator raise important questions concerning previous interpretations of the physical mechanisms responsible for producing internal, interdecadal variability in idealized OGCMs (e.g., [Cai 1995](#); [Cai et al. 1995](#); [Chen and Ghil 1995](#); [Greatbatch and Zhang 1995](#); [Huang and Chou 1994](#); [Winton 1996](#)). In particular, whether the oscillatory mechanism of an OGCM is dependent on an interaction between adjustment and advective processes and the importance of the deep-ocean temperature anomalies needs to be determined.

In summary, by simply reformulating the parameterization of WS to include a TC adjustment timescale comparable to that of the advective timescale, interdecadal oscillations in a zonally averaged ocean model forced by a time-independent heat flux have been documented that may be related to the interdecadal variability simulated by OGCMs. While the oscillatory mechanism needs to be verified with an OGCM, the results strongly suggest that internal, interdecadal variability of the large-scale meridional overturning of the Atlantic Ocean is not an inherently nonlinear or three-dimensional phenomenon and that this type of variability cannot be idealized as a loop oscillator.

#### Acknowledgments

JD was supported by an East–West Center Fellowship and NASA Global Climate Change Fellowship during this research. FFJ was partially supported by NSF Grant ATM-9312888 and by NOAA Grant GC95773. The comments provided by two anonymous reviewers were useful in the improvement of this manuscript.

---

#### REFERENCES

- Cai, W., 1995: Interdecadal variability driven by mismatch between surface flux forcing and oceanic freshwater/heat transport. *J. Phys. Oceanogr.*, **25**, 2643–2666..
- , R. J. Greatbatch, and S. Zhang, 1995: Interdecadal variability in an ocean model driven by a small, zonal redistribution of the surface buoyancy flux. *J. Phys. Oceanogr.*, **25**, 1998–2010..
- Chen, F., and M. Ghil, 1995: Interdecadal variability of the thermohaline circulation and high-latitude surface fluxes. *J. Phys. Oceanogr.*, **25**, 2547–2568..
- Delworth, T., S. Manabe, and R. J. Stouffer, 1993: Interdecadal variations of the thermohaline circulation in a coupled ocean–atmosphere model. *J. Climate*, **6**, 1993–2011.. [Find this article online](#)
- Dewar, W. K., and R. X. Huang, 1995: Fluid flow in loops driven by freshwater and heat fluxes. *J. Fluid Mech.*, **297**, 153–191..
- Döscher, R., C. W. Böning, and P. Herrmann, 1994: Response of circulation and heat transport in the North Atlantic to changes in thermohaline forcing in northern latitudes: A model study. *J. Phys. Oceanogr.*, **24**, 2306–2320..
- Greatbatch, R. J., and S. Zhang, 1995: An interdecadal oscillation in an idealized ocean basin forced by constant heat flux. *J. Climate*, **8**, 81–91.. [Find this article online](#)
- , and K. Peterson, 1996: Interdecadal variability and oceanic thermohaline adjustment. *J. Geophys. Res.*, **101**, 467–20 482..
- Hasselmann, K., 1991: Ocean circulation and climate change. *Tellus*, **43A**, 82–103..
- Huang, R. X., and R. L. Chou, 1994: Parameter sensitivity study of the saline circulation. *Climate Dyn.*, **9**, 391–409..
- Kushnir, Y., 1994: Interdecadal variations in North Atlantic sea surface temperature and associated atmospheric conditions. *J. Climate*, **7**, 141–157.. [Find this article online](#)
- Manabe, S., and R. J. Stouffer, 1988: Two stable equilibria of a coupled ocean–atmosphere model. *J. Climate*, **1**, 841–866.. [Find this article](#)



[online](#)

Marotzke, J., 1994: Ocean models in climate problems. *Ocean Processes in Climate Dynamics: Global and Mediterranean Examples*, P. Malanotte-Rizzoli and A. R. Robinson, Eds., Kluwer Academic, 79–109..

—, P. Welander, and J. Willebrand, 1988: Instability and multiple steady states in a meridional-plane model of the thermohaline circulation. *Tellus*, **40A**, 162–172..

Rooth, C., 1982: Hydrology and ocean circulation. *Progress in Oceanography*, Vol. 11, 131–149..

Stocker, T. F., and L. A. Mysak, 1992: Climatic fluctuations on the century time scale: A review of high-resolution proxy data and possible mechanisms. *Climate Change*, **20**, 227–250..

Winton, M., 1996: The role of horizontal boundaries in parameter sensitivity and decadal-scale variability of coarse-resolution ocean general circulation models. *J. Phys. Oceanogr.*, **26**, 289–304..

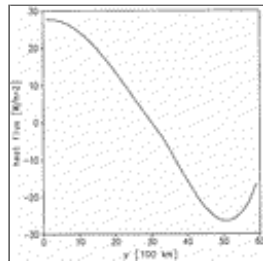
—, and E. S. Sarachik, 1993: Thermohaline oscillations induced by strong steady salinity forcing of ocean general circulation models. *J. Phys. Oceanogr.*, **23**, 1389–1410..

Wright, D. G., and T. F. Stocker, 1991: A zonally averaged ocean model for the thermohaline circulation. Part I: Model development and flow dynamics. *J. Phys. Oceanogr.*, **21**, 1713–1724..

—, C. B. Vreugdenhil, and T. M. C. Hughes, 1995: Vorticity dynamics and zonally averaged ocean circulation models. *J. Phys. Oceanogr.*, **25**, 2141–2154..

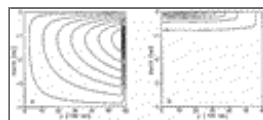
Yang, J., and J. D. Neelin, 1993: Sea-ice interaction with the thermohaline circulation. *Geophys. Res. Lett.*, **20**, 217–220..

## Figures



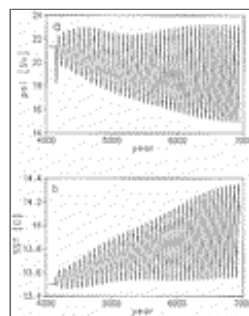
[Click on thumbnail for full-sized image.](#)

Fig. 1. Surface heat flux ( $\text{W m}^{-2}$ ) diagnosed from the stationary state ([Fig. 2](#)) reached by restoring SST to  $T^*$ .



[Click on thumbnail for full-sized image.](#)

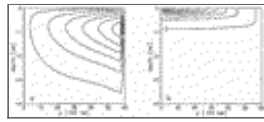
Fig. 2. Stationary state reached by restoring SST to  $T^*$ . (a) Streamfunction; contour interval is 3 Sv. (b) Temperature; contour interval is  $3^\circ\text{C}$ .



[Click on thumbnail for full-sized image.](#)

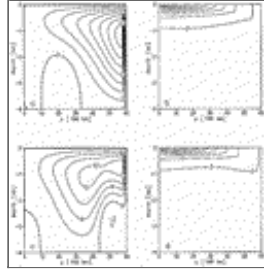
Fig. 3. Evolution of (a) maximum overturning (Sv) and (b) basin-mean SST ( $^\circ\text{C}$ ) after restarting the integration from the

equilibrium state (Fig. 2) with a diagnosed heat flux (Fig. 1) rather than a restoring condition as the thermal boundary condition. Note that a  $+0.2^{\circ}\text{C}$  temperature anomaly was added to the upper 500 m poleward of  $40^{\circ}$  at year 4100 to nudge the system away from the unstable stationary state.



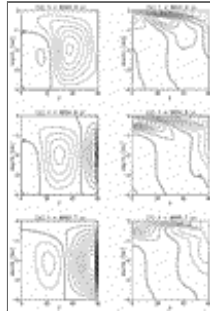
[Click on thumbnail for full-sized image.](#)

Fig. 4. Time-mean state. (a) Streamfunction; contour interval is 3 Sv. (b) Temperature; contour interval is  $3^{\circ}\text{C}$ .



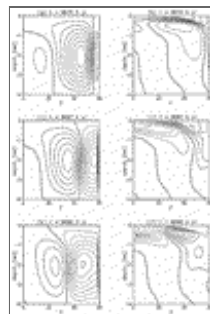
[Click on thumbnail for full-sized image.](#)

Fig. 5. Extreme phases of the oscillation. (a) Maximum overturning and corresponding (b) temperature; (c) minimum overturning and (d) corresponding temperature. Contour intervals are 3 Sv and  $3^{\circ}\text{C}$ .



[Click on thumbnail for full-sized image.](#)

Fig. 6. Anomalous (a, c, e, g, i, k) streamfunction and (b, d, f, h, j, l) temperature in 10.9-yr intervals spanning one complete oscillation. Contour intervals are 1 Sv and  $0.1^{\circ}\text{C}$  with solid, dashed, and bold dashed lines denoting positive, negative, and zero anomalies respectively.



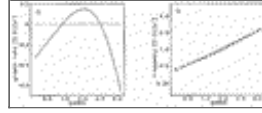
[Click on thumbnail for full-sized image.](#)

Fig. 6. (Continued)



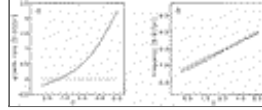
Click on thumbnail for full-sized image.

Fig. 7. Spatial characteristics of the (a, c, e) streamfunction and (b, d, f) temperature at intervals of  $\pi/3$  (9 yr) for the leading mode with the linearized inertial terms neglected. Contour intervals are consistent with those of Fig. 6 (1 Sv and 0.1°C) with solid and dashed lines denoting positive and negative anomalies, respectively. The zero contour is represented by a bold dashed line.



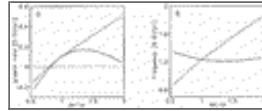
Click on thumbnail for full-sized image.

Fig. 8. Dependence of the leading mode on  $\gamma$ . (a) Growth rate  $(100 \text{ yr})^{-1}$  and (b) frequency  $(100 \text{ yr})^{-1}$ ; dashed line represents a slope of 0.5.



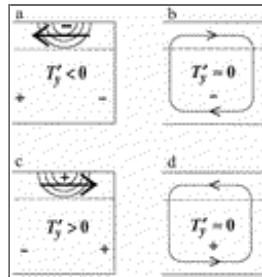
Click on thumbnail for full-sized image.

Fig. 9. Dependence of the leading mode on  $c$ . (a) Growth rate  $(100 \text{ yr})^{-1}$  and (b) frequency  $(100 \text{ yr})^{-1}$ ; dashed line represents a slope of 0.5.



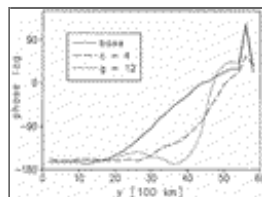
Click on thumbnail for full-sized image.

Fig. 10. Dependence of the leading mode on the basic-state overturning intensity (solid line) and density stratification (dashed line). (a) Growth rate  $(100 \text{ yr})^{-1}$  and (b) frequency  $(100 \text{ yr})^{-1}$ .



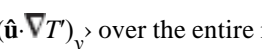
Click on thumbnail for full-sized image.

Fig. 11. Schematic diagram of the oscillatory mechanism near the sinking region. A plus (minus) represents a local maximum (minimum) temperature anomaly throughout the entire upper or deep ocean. The larger magnitude of the upper-ocean  $T'$  compared to deep-ocean  $T'$  is denoted by the half circles. Overturning anomalies are represented by the ovals with the direction of anomalous overturning denoted by an arrowhead. The forcing of the temperature gradient anomaly by the basic-state advection of  $T'$  is represented by a bold arrow with the direction denoting the sign of the forcing. The dashed line separates the ocean into two distinct regions based on the temperature structure of the basic state. In the upper 1000 m,  $\hat{T}'_y < 0$ , and  $\hat{T}'_z > 0$ , whereas  $\hat{T}'_y \approx \hat{T}'_z \approx 0$  in the lower 3000 m.

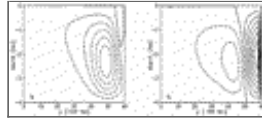


Click on thumbnail for full-sized image.

Fig. 12. Phase lag in degrees between  $\langle T'_y \rangle$  and  $\langle -(\hat{\mathbf{u}} \cdot \nabla T')_y \rangle$  over the entire model domain for the base,  $c = 4$ , and  $\gamma = 12$



oscillations. Positive values denote  $\langle T'_y \rangle$  lagging  $\langle -(\hat{\mathbf{u}} \cdot \nabla T)_y \rangle$ .



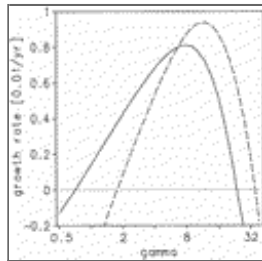
Click on thumbnail for full-sized image.

Fig. 13. Spatial characteristics of the streamfunction for the leading mode with  $\gamma = 12$  ( $c = 1$ ) at an interval of  $\pi/3$  (6.4 yr). The contour interval is arbitrary with solid and dashed lines denoting positive and negative anomalies respectively. Note the stronger damping of  $\Psi'$  in the vicinity of  $y = 40^\circ$  from (a) to (b) compared to that of the base oscillation (Figs. 7a,c).



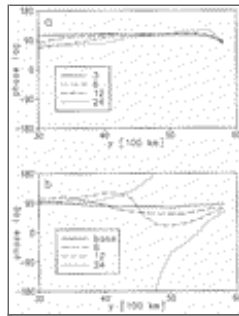
Click on thumbnail for full-sized image.

Fig. 14. Phase diagram of  $\langle T'_y \rangle$  (temperature gradient) and  $\langle -(\hat{\mathbf{u}} \cdot \nabla T)_y \rangle$  (advection) at  $y = 50^\circ$  (solid line) and  $y = 40^\circ$  (dashed line) for the (a) base, (b)  $c = 4$ , and (c)  $\gamma = 12$  oscillations. Units of  $\langle T'_y \rangle$  and  $\langle -(\hat{\mathbf{u}} \cdot \nabla T)_y \rangle$  can be taken as some multiple of  $^\circ\text{C}$  and  $^\circ\text{C yr}^{-1}$  respectively.



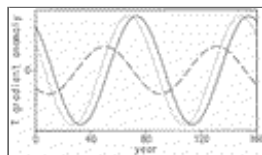
Click on thumbnail for full-sized image.

Fig. 15. Dependence of the growth rate  $(100 \text{ yr})^{-1}$  on  $\gamma$  with horizontal viscosity neglected ( $A_h = 0$ ). Solid and dashed lines denote the basic-state circulation set to the stationary state (Fig. 2a) and double the stationary state respectively.



Click on thumbnail for full-sized image.

Fig. 16. Phase lag in degrees between  $\langle -T'_y \rangle$  and  $\langle \mathbf{V}'_u \rangle$  for variations in  $\gamma$  for (a)  $A_h = 0$  and (b) standard conditions. Positive values denote  $\langle \mathbf{V}'_u \rangle$  lagging  $\langle -T'_y \rangle$ .



Click on thumbnail for full-sized image.

Fig. 17. Relative contribution of  $\langle T'_y \rangle_u$  (dashed line) and  $\langle T'_y \rangle_d$  (solid line) to  $\langle T'_y \rangle$  (dotted line) at  $y = 50^\circ$  for the base oscillation.

Corresponding author address: Mr. Jeff Drbohlav, Department of Meteorology, University of Hawaii at Manoa, 2525 Correa Road, Honolulu, HI 96822.

E-mail: [jeffd@soest.hawaii.edu](mailto:jeffd@soest.hawaii.edu)

[top](#) ▲



© 2008 American Meteorological Society [Privacy Policy and Disclaimer](#)  
Headquarters: 45 Beacon Street Boston, MA 02108-3693  
DC Office: 1120 G Street, NW, Suite 800 Washington DC, 20005-3826  
[amsinfo@ametsoc.org](mailto:amsinfo@ametsoc.org) Phone: 617-227-2425 Fax: 617-742-8718  
[Allen Press, Inc.](#) assists in the online publication of *AMS* journals.